Growth of cobalt films at room temperature using sequential exposures of cobalt tricarbonyl nitrosyl and low energy electrons

Zachary C. Sobell, Andrew S. Cavanagh, and Steven M. George
Department of Chemistry, University of Colorado, Boulder, Colorado 80309

(Received 6 June 2019; accepted 16 September 2019; published 15 October 2019)

Cobalt thin films were grown at room temperature using sequential exposures of cobalt tricarbonyl nitrosyl (CTN, $Co(CO)_3NO$) and low energy (75–175 eV) electrons. During this cyclic growth process, the CTN molecules were first adsorbed on the substrate. The electrons then induced the desorption of the carbonyl and nitrosyl ligands from the adsorbed CTN. The removal of CO and NO ligands produced new adsorption sites. Subsequent CTN exposures allowed CTN to react with these new adsorption sites on the substrate. *In situ* ellipsometry was utilized to monitor the film thickness during the electron enhanced growth. Co growth rates as high as 1.3 Å/cycle were observed by *in situ* ellipsometry depending on the reaction conditions. The *in situ* ellipsometry also observed the CTN adsorption and the removal of the carbonyl and nitrosyl ligands. Quadrupole mass spectrometer measurements confirmed the desorption of CO and NO during electron exposures. X-ray photoelectron spectroscopy (XPS) measured N XPS signals from the Co films deposited using electron exposures at 200 eV. The N/Co XPS signal ratio was consistent with the dissociation of 13% of the nitrosyl ligands on the CTN precursors that lead to Co deposition. In contrast, the negligible C XPS signals from the Co films indicated that the CO ligands were desorbed completely from CTN by the electron exposures at 200 eV. Under identical reaction conditions at lower incident electron currents, the maximum growth rate was obtained at an electron energy of 125 eV. Because the Co growth depends on the electron flux, the Co films were deposited only on the surface area irradiated by the electron beam. The spatial profile of the Co film deposited using long electron exposure times was mapped by *ex situ* spectroscopic ellipsometry. This spatial profile displayed a pronounced flat top that was consistent with the electron flux desorbing nearly all the CO and NO surface coverage in the central area of the electron beam during each reaction cycle. The spatial profile was used to calculate an electron induced desorption cross section of $\sigma = 2 \times 10^{-17}$ cm^2 at 200 eV. This cross section was in approximate agreement with the cross sections for the electron impact dissociation of CTN in the gas phase. *Published by the AVS.* https://doi.org/10.1116/1.5113711

I. INTRODUCTION

Electrons are able to enhance surface reactions by a number of pathways including electron stimulated desorption (ESD), dissociative electron attachment (DEA), and electron induced dissociation (EID).[1] These electron induced processes can dramatically reduce the temperature for thin film growth. These processes can also be employed for nanofabrication using focused electron beam induced deposition (FEBID).[1] There are many unanswered questions on the exact mechanism for electron enhanced reactions and the dependence of these reactions on electron energy.[2] Although high electron energies >1 keV are typically utilized for FEBID, the secondary electrons with energies <50 eV may be the most effective in inducing the surface reactions.[2–4]

ESD can enhance thin film growth by removing surface species that limit surface reactions. ESD can occur by a number of pathways including the Menzel–Gomer–Redhead (MGR)[5] and the Knotek–Feibelman (KF)[6] mechanisms. The MGR mechanism is characterized by the promotion of a bonding electron to an antibonding orbital that leads to the scission of the bond. In contrast, the KF mechanism is an Auger process. An incident electron can remove a core electron, and then, an electron from a higher energy level can drop down to replace the ejected electron. Energy conservation leads to another electron being ejected from the system together with ligand desorption.

DEA can also enhance surface reactions by promoting the decomposition of the reactant.[3,7] DEA is usually observed with low energy electrons <10 eV. These low energy electrons can be produced by secondary electrons. The reactant can capture a low energy electron and form a transient negative ion. This transient negative ion can either relax through reemission of the electron or dissociate to produce an anion and a neutral species.

EID can also enhance surface reactions by causing the dissociation of the reactant.[3,8] The dissociation could occur by dissociative ionization where the electron removes a bound electron from the reactant and forms a cation. The cation can then undergo fragmentation to produce various dissociation products. The dissociation could also occur by neutral dissociation resulting from electronic excitation. The excited neutral may then decompose to neutral fragments if the potential energy surface is repulsive.

Previous studies have shown that thin films can be deposited at room temperature using sequential surface reactions with low energy electrons. For example, GaN films can be

Note: This paper is part of the 2020 Special Topic Collection on Atomic Layer Deposition (ALD).

grown at room temperature with a sequential surface reaction approach similar to atomic layer deposition (ALD).[9] This GaN film growth was performed using sequential $Ga(CH_3)_3$, NH_3, and electron exposures. Hydrogen radical beam exposures after the $Ga(CH_3)_3$ exposures were able to replace the CH_3 groups with H surface species. The low energy electrons led to hydrogen desorption and produced new adsorption sites. GaN growth rates of 1.3 Å/cycle were measured at electron energies of 50 eV.[9]

Si films have also been deposited at room temperature using sequential Si_2H_6 and low energy electron exposures.[10] The Si electron enhanced ALD (EE-ALD) growth occurred at electron energies from 25 to 200 eV. The low energy electrons were able to desorb hydrogen and produce new adsorption sites. The Si growth was self-limiting and saturated at longer Si_2H_6 and electron exposures. The maximum Si EE-ALD growth rate of 0.3 Å/cycle was observed at 100–150 eV.[10]

BN films have also been deposited at room temperature using sequential borazine ($B_3N_3H_6$) and low energy electron exposures.[11] The BN EE-ALD growth occurred at electron energies from 40 to 440 eV and saturated at longer borazine and electron exposures. The maximum BN EE-ALD growth rate of 3.2 Å/cycle was observed at 80–160 eV.[11] This growth rate was nearly identical to the distance between neighboring BN basal planes in hexagonal BN. In addition, the BN EE-ALD displayed topographical selectivity and preferentially deposited on horizontal surfaces when the electron beam was normal to the surface.[11] These area-selective EE-ALD results suggested that EE-ALD could be employed for "bottom-up fill" of vias and trenches with vertical sidewalls.

In the current paper, Co thin films were grown using sequential cobalt tricarbonyl nitrosyl (CTN, $Co(CO)_3NO$) and low energy electron exposures. Cobalt is emerging as an important interconnect material to replace copper or tungsten.[12,13] The ability to deposit cobalt in vias and trenches using a "bottom-up fill" mechanism would be desirable to avoid voids and grain boundaries in the conducting lines. CTN is a common cobalt precursor utilized for Co chemical vapor deposition (CVD) at temperatures from 150 to 480 °C.[14,15] The highest purity Co CVD films have been deposited at 350–480 °C.[14] CTN is also used to fabricate Co nanostructures using FEBID techniques.[16–18]

Many investigations have explored the mechanisms involved during Co deposition using CTN with FEBID techniques. The role of low energy electrons and the DEA process during Co deposition using CTN have been examined by several studies.[3,7,19] These investigations conclude that the DEA pathway is non-negligible and leads to incomplete CTN decomposition. Other studies have examined the EID and electron induced ionization of CTN in the gas phase.[20–22] These investigations have measured absolute cross sections for the electron induced processes versus electron energy.[22] These gas phase studies versus electron energy are useful to compare with the Co FEBID results versus electron energy to determine the effect of the surface. Additional investigations have examined the individual steps during CTN decomposition by FEBID using surface analytical techniques such as x-ray photoelectron spectroscopy (XPS) and quadrupole mass spectrometry (QMS).[17]

This study investigated Co thin film growth using sequential exposures of CTN and low energy electrons from 75 to 175 eV. The growth of the Co films versus the number of reaction cycles was examined in an ultrahigh vacuum (UHV) chamber using *in situ* ellipsometry. The *in situ* ellipsometry measurements were able to monitor the CTN adsorption and the subsequent desorption of ligands during the electron beam exposure. QMS analysis was also used to determine that CO and NO were desorbed into the gas phase during electron exposures. Additional *ex situ* spectroscopic ellipsometer experiments were used to map the spatial profile of the Co film formed by the area-selective electron beam. This spatial profile was also utilized to determine the electron induced desorption cross section at 200 eV.

II. EXPERIMENT

A. Vacuum chamber

Metallic Co films were grown in a UHV chamber described previously.[10,11] The chamber contains a load lock with a Pirani gauge and a hot cathode gauge as pressure sensors. The load lock includes an integrated UV light source to desorb water from the sample, sample holder, and walls of the load-lock chamber. The load lock is pumped with a turbomolecular pump with a pumping speed of 67 l/s backed by a rotary vane pump. The load lock is separated from the main chamber by a UHV gate valve. The main chamber is pumped by two turbomolecular pumps, one operating at 245 l/s, backed by a smaller turbomolecular pump operating at 67 l/s that is backed by a rotary vane pump. Additionally, the main chamber is pumped by an ion pump operating at 80 l/s with a valve used to close the ion pump off to process gases.

The main chamber has both hot and cold cathode pressure sensors (MKS), as well as an *in situ* ellipsometer (Filmsense1), a mass spectrometer (PrismaPlus QMG 220, Pfeiffer Vacuum), and a picoammeter (Keithley) attached to the sample stage to measure the incident electron current. Attached to the main chamber, separated by another UHV gate valve, is an analysis chamber equipped with an ion pump with a pumping speed of 75 l/s and an *in situ* Auger electron spectroscopy (AES) spectrometer.

B. Growth procedure

Si wafers (Silicon Valley Microelectronics, boron doped) were washed in methanol and acetone and blown dry with ultrahigh purity nitrogen. There was no attempt to remove the native oxide on the silicon surface. The Si wafer was then loaded into the load lock chamber. The pressure was reduced to $\sim 10^{-6}$ Torr, and then the UV light was activated for 90 min to desorb water. Upon pressure reduction to $\sim 10^{-8}$ Torr, the load lock was opened to the main chamber, and the sample was transferred to the sample stage that was positioned normal to the electron gun. The sample was further irradiated with UV light for 30 min, while the main

chamber pumped down to at least 1×10^{-9} Torr before the first precursor exposure.

The Co growth was conducted using a pulse sequence consisting of (1) CTN adsorption, (2) purging, (3) electron gun warm up, (4) electron gun exposure, and (5) electron gun cool down. The timing for this pulsing sequence can be characterized by (t_1, t_2, t_3, t_4, and t_5). The CTN precursor was kept at 1.5 Torr behind a micropulse valve. The valve was actuated for $t_1 = 0.1$ s. The valve opening led to a transient pressure in the main chamber of $\sim 7.5 \times 10^{-6}$ Torr. A purge was then performed for a total of $t_2 = 75$ s. An additional $t_3 = 50$ s was required for the filament of the electron flood gun to warm up. A typical electron exposure was then performed at 100 eV for $t_4 = 240$ s, with an emission current of 100 μA. Another delay time of $t_5 = 175$ s was introduced to allow the cooling of the electron gun filament. The timing for this pulsing sequence was 0.1, 75, 50, 240, and 175. The sum of these steps produced a reaction cycle time of 540 s or 9 min.

C. Electron flood gun

The Co film growth was observed using low energy (75–175 eV) electrons from an electron flood gun. The electron flood gun was a model FRA-2×1-2 from Kimball Physics Inc. The filament was a tantalum disc mounted on a tungsten-rhenium (95%–5%) support. The electron gun was capable of producing electron energies of 5–1000 eV and emission currents of 1 nA to 400 μA. The grid voltage was set at 100 V. To preserve the filament and avoid overcurrent conditions, the emission current was maintained at 100 μA.

The total emission current of 100 μA was not incident on the sample. The picoammeter measured incident electron currents on the sample that were less than the emission current of 100 μA. Most of the loss of the electron current occurs on the grounded anode of the electron gun. During earlier experiments when larger Co growth rates of 1.0–1.3 Å/cycle were measured at electron energies of 125–150 eV, the incident electron currents were 33–45 μA. During later experiments after many Co deposition experiments when smaller Co growth rates were measured at similar electron energies, the incident electron currents were lower at 24–28 μA. The lower incident electron currents are attributed to the effect of Co deposition on the grid and the anode of the electron gun.

D. Ellipsometry and XPS analysis

In situ ellipsometry (Filmsense, FS1) measurements were performed in duplicate after each electron exposure. The *in situ* ellipsometer uses four wavelengths of light. The measurements were averaged to obtain the growth per cycle (GPC). The precision of the *in situ* ellipsometry measurements of the film thickness is within ±0.03 Å.

Ex situ spectroscopic ellipsometry (Model M-2000, J.A. Woollam Co., Inc.) was performed to obtain the n and k values, measure the film thickness, and determine the spatial profile of the deposited film. The data were fit using a B-spline model in CompleteEase (J.A. Woollam Co., Inc.) with n and k values for Co as a starting point. Focusing probes that reduce the spot size to 0.3–0.4 mm were used for all data acquisition.

The film composition was determined using an x-ray photoelectron spectrometer (PHI 5600) using a monochromatic Al Kα source with an energy of 1486.6 eV. The pass energy was 29.35 eV, and the step size was 0.25 eV. An electron beam neutralizer was used during the XPS measurements. The XPS data were collected using Auger Scan (RBD Instruments) software. The XPS data were analyzed in CASA XPS (Casa Software Ltd.) software.

III. RESULTS AND DISCUSSION

A. Nucleation, growth, and observation of precursor adsorption and ligand desorption

The nucleation and growth of a Co film on the native oxide of a silicon wafer at room temperature were measured using *in situ* ellipsometry as shown in Fig. 1. The Co film growth was conducted at an electron energy of 150 eV. The timing for the pulsing sequence was 0.1, 75, 50, 120, and 175. The electron current from the filament was 100 μA. The incident electron current on the sample was 33 μA. The *in situ* ellipsometry measurements were conducted after each reaction cycle. Figure 1 shows that there is very little Co deposition during the first 10 reaction cycles. The film growth then begins to occur at >10 reaction cycles. After >55 reaction cycles, the Co film is growing linearly at a rate of 1.3 Å/cycle.

The nucleation delay is likely caused by the lack of active sites on the native oxide of the silicon wafer. Repeated cycles of CTN adsorption followed by electron exposures slowly build up active Co sites on the surface. These Co sites probably first form small islands, and then the islands may grow together as described by the Volmer–Weber mechanism.[23] This behavior has been observed by previous nucleation studies of metal ALD on oxide surfaces.[24] After a continuous

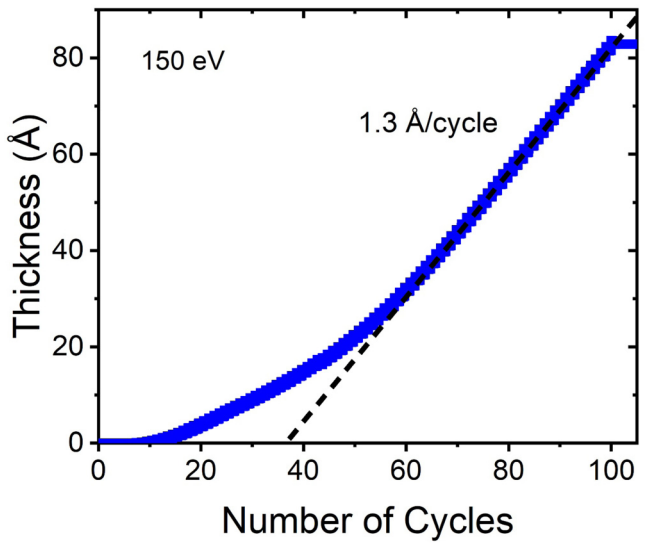

FIG. 1. Film thickness measured by *in situ* ellipsometry vs the number of reaction cycles during Co growth on native oxide on an Si wafer.

Co film forms on the surface, there will be a full coverage of active sites on the surface. At this point, the Co deposition reaches the steady state, linear growth regime. To achieve a more rapid nucleation, experiments could also be performed on H-passivated Si surfaces. Earlier Si EE-ALD experiments have demonstrated that hydrogen can be desorbed from Si surfaces by low energy electron exposures.[10] The active sites produced by hydrogen desorption are expected to be very reactive and should facilitate prompt nucleation.

An expansion of the *in situ* ellipsometry measurements displayed in Fig. 1 reveals the individual events during the sequential CTN and electron exposures. Figure 2 shows the film thickness measured during six reaction cycles from Fig. 1. The individual ellipsometry measurements were performed every 10 s. The rapid increase in the thickness observed in Fig. 2 occurs when the CTN precursor is dosed into the chamber and adsorbs on the surface. Subsequently, the thickness decreases slowly during the purge following the CTN exposure. The thickness then decreases rapidly at the onset of the electron exposure and resulting electron induced desorption from the surface. The thickness then is constant during the delay time after the electron exposure.

The decrease in the thickness shown in Fig. 2 during the onset of the electron exposure corresponds with the desorption of CO and NO ligands from CTN adsorbed on the surface. To confirm the desorption of CO and NO, QMS was used to monitor the gas phase during the reaction cycle. For these experiments, the electron energy was 100 eV. The electron current from the filament was 100 μA. The incident electron current on the sample was 45 μA. Each reaction cycle had a timing for the pulse sequence of 0.1, 75, 50, 60, and 175. Figure 3 shows the QMS results at m/z = 28, 30, and 173 corresponding with CO, NO, and $Co(CO)_3NO$.

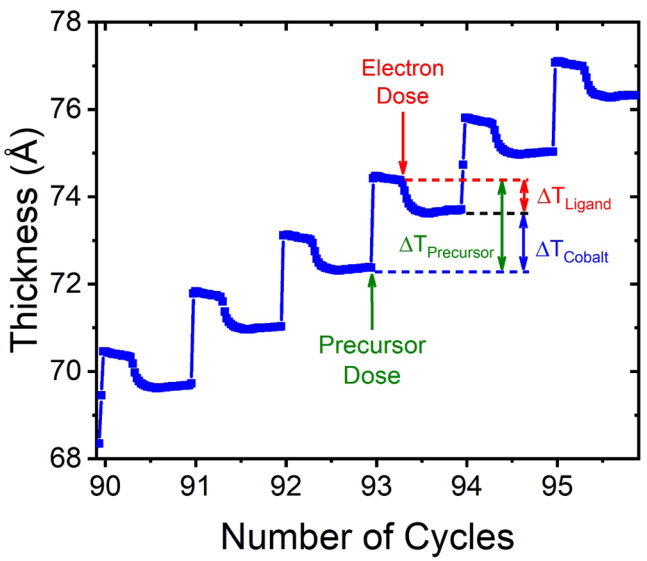

FIG. 2. Expansion of film thickness measured by *in situ* ellipsometry for six reaction cycles. Expansion shows a thickness increase during CTN adsorption, a thickness loss during electron beam exposure when CO and NO ligands are removed, and nearly constant thicknesses during purge times after CTN and electron beam exposures.

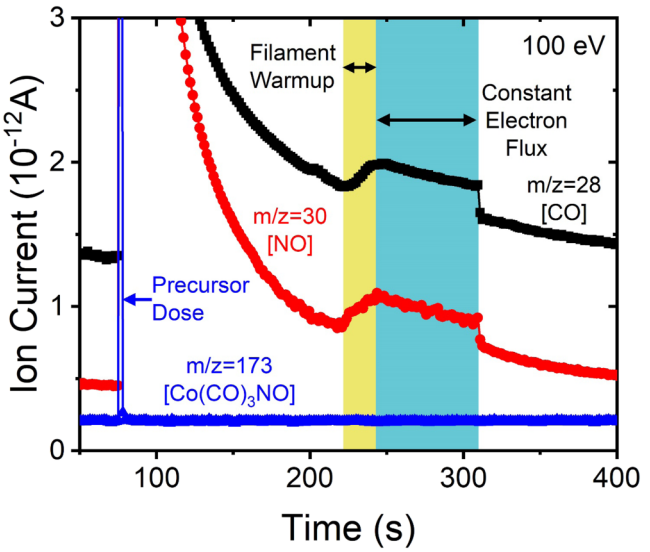

FIG. 3. Partial pressures of CO, NO, and parent molecule, CTN, as recorded by quadrupole mass spectrometer during sequential CTN exposure, purge time after CTN exposure, electron exposure, and a delay time after electron exposure.

Figure 3 shows that the ion currents for m/z = 28, 30, and 173 are high during the CTN exposure that occurs at 75 s. These masses are all part of the mass spectrometry fragmentation pattern for CTN.[20,21] The ion current for m/z = 173 is present only during the CTN exposure. The ion currents for m/z = 28 and 30 persist during the pumping period following the CTN exposure. They decrease as expected for the pumping of NO and CO from the chamber.

The electron beam exposure that occurs at 220 s then increases the ion currents only for m/z = 28 and 30 corresponding to CO and NO. There is no ion current for CTN at m/z = 173. These ion currents increase slowly during the initial electron emission from the electron filament. These ion currents then slowly decrease again after the electron emission current has reached its final value of 100 μA at 245 s. The ion currents for m/z = 28 and 30 then decrease rapidly when the electron emission current is stopped at 320 s. The ion currents continue to decrease because of pumping during the delay time after the electron exposure.

Additional QMS experiments were performed at higher electron energies of 400 eV. Ion currents were again observed for m/z = 28 and 30 corresponding to CO and NO desorption from the surface. However, no peaks were observed at m/z = 173 from CTN or at m/z = 59 from possible Co etching products. These results are in contrast to earlier results for the GaN electron enhanced growth where Ga-containing etch products were observed to desorb at greater abundance at higher electron energies.[9]

These QMS results can also be compared with earlier QMS investigations of electron irradiation of CTN multilayer films.[17] These CTN multilayer films had a thickness of ~2.5 nm and were adsorbed on gold substrates at −168 °C. Upon electron irradiation at an electron energy of 500 eV, CO and negligible NO were observed in the gas phase.[17] In addition, there was no evidence of any Co-containing

species in the gas phase. The lack of NO in the gas phase during electron irradiation was consistent with dissociation of the NO ligands in the CTN multilayer films at electron energies of 500 eV.[17] In contrast, NO and CO are both added to the gas phase during electron exposures at 100 eV shown in Fig. 3. QMS measurements at m/z = 32 also observed no O_2 in the gas phase during electron exposures at 100 eV.

B. Electron energy dependence of film growth

The Co film growth was also examined using different electron energies. These experiments were performed after many previous Co deposition experiments. The results for electron energies of 75, 100, 125, 150, and 175 eV are displayed in Fig. 4. The timing of the pulsing sequence was 0.1, 75, 50, 240, and 175. The electron current from the filament was 100 μA. For these experiments, the electron current incident on the sample was lower at 24–28 μA. The *in situ* ellipsometry measurements were again conducted after each reaction cycle. There is no nucleation period because the Co film growth was conducted on a previous Co film for each electron energy.

The Co film growth per cycle (GPC) is dependent on electron energy. The GPC is not in saturation at these lower incident electron currents and relatively short electron exposure times. Under saturating, self-limiting growth conditions, the GPC would have been constant versus electron energy. The GPC is 0.18 Å/cycle at 75 eV. The GPC increases with electron energy and reaches a maximum GPC of 0.50 Å/cycle at 125 eV. The GPC at higher electron energies is then reduced to a GPC of 0.34 Å/cycle at 150 eV and 0.21 Å/cycle at 175 eV. The GPC values versus electron energy are summarized in Fig. 5.

The GPC of 0.34 Å/cycle at 150 eV is lower than the GPC of 1.3 Å/cycle at 150 eV observed in Figs. 1 and 2. Although the electron current from the filament was the same at 100 μA, the incident electron currents at the sample were lower at 24–28 μA. These lower electron currents may have been caused by changes to the electron gun resulting from Co deposition. The CTN can adsorb on the surfaces of the electron gun at room temperature. Over multiple Co deposition experiments, Co will deposit on the grid and the anode of the electron gun. This Co deposition may alter the electron current from the electron gun. The lower growth rate of 0.34 Å/cycle at 150 eV is attributed to the lower incident electron currents.

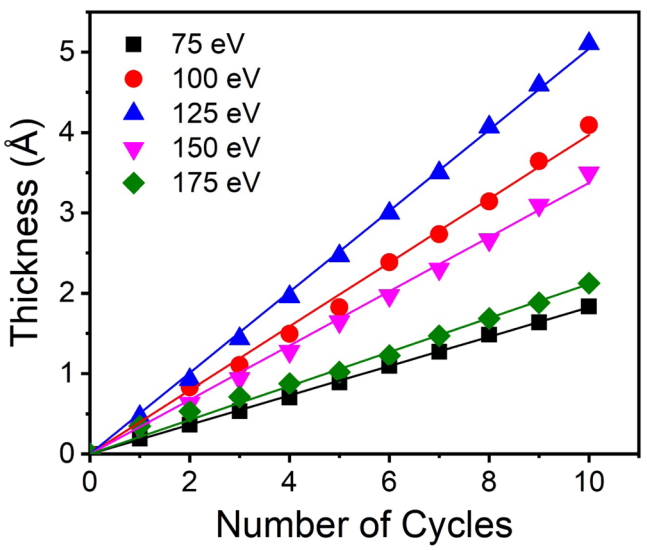

FIG. 4. Film thickness measured by *in situ* ellipsometry vs the number of reaction cycles during Co growth at various electron energies.

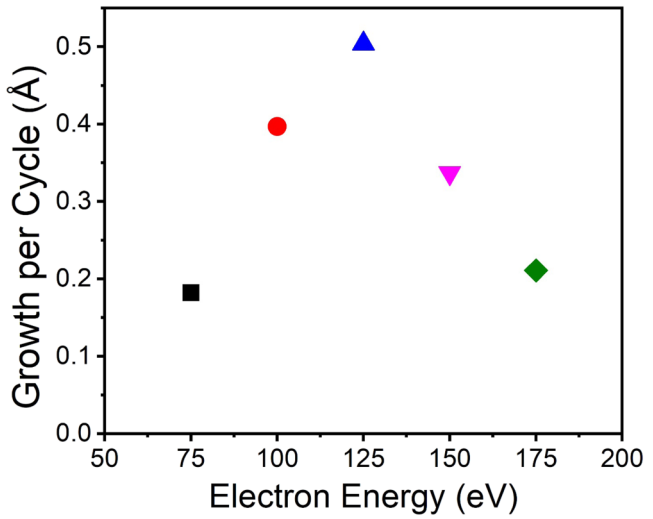

FIG. 5. Summary of growth per cycle for Co growth vs electron energies. The maximum growth per cycle occurs at 125 eV.

C. Spatial distribution of film deposition

The Co film was also readily observed on the Si wafer. A picture of the Co film on the Si wafer is shown in Fig. 6. This Co film was deposited using 223 reactions cycles at room temperature. The electron energy was 100 eV. Each

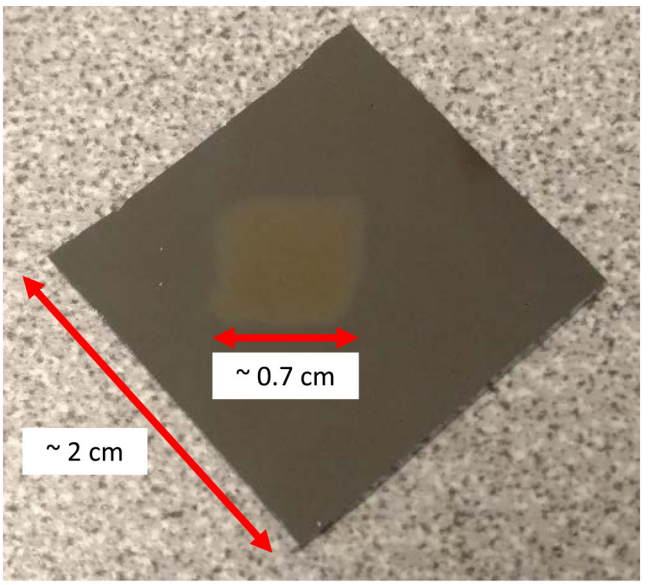

FIG. 6. Picture of the Co film on a silicon wafer after 223 reaction cycles with an electron energy of 100 eV. Area-selective deposition limits the Co film to a diameter of ~7 mm.

reaction cycle had a timing for the pulse sequence of 0.1, 75, 50, 60, and 175. The electron current from the filament was 100 μA. The incident electron current on the sample was 45 μA. The Co film is selectively deposited where the electron current was incident on the Si wafer. The Co film has a shiny silver-tan color. The thickness of this Co film measured using *ex situ* ellipsometry was 110 Å. Assuming a nucleation period that may vary from 20 to 45 cycles, this film thickness is consistent with a growth rate ranging from 0.54 to 0.62 Å/cycle at 100 eV. The diameter of the Co film is approximately 7 mm.

The film thickness could also be profiled using *ex situ* spectroscopic ellipsometry. The results for one of these spatial profiles are displayed in Fig. 7. This Co film was deposited using 198 reaction cycles at room temperature. The electron energy was 200 eV. Each reaction cycle had a timing for the pulse sequence of 0.1, 75, 50, 960, and 175. The electron current from the filament was 100 μA. The incident electron current on the sample was 21 μA. The diameter of the Co film deposition is ~7 mm in agreement with the picture of the Co film in Fig. 6.

In addition, the top of the spatial profile in Fig. 7 has a flat top. This flat top indicates that the electron induced desorption has reached saturation and removed nearly all of the CO and NO ligands over the central portion of the electron beam. Similar flat top spatial profiles were observed in previous studies of Si EE-ALD and BN EE-ALD.[10,11] Based on an average of nine points at the flat top of the spatial profile in Fig. 7, the thickness at the flat top was 289 Å with a standard deviation of ±10 Å.

This film thickness of 289 Å can be used to estimate a Co growth rate. The nucleation period may be shorter at the long electron exposure times of 960 s per reaction cycle utilized for the film growth shown in Fig. 7. Assuming a nucleation period of ~20 cycles, this film thickness of 289 Å is consistent with a growth rate of 1.6 Å/cycle at 200 eV. Assuming no nucleation period yields a growth rate of 1.5 Å/cycle. This high growth rate at 200 eV may be attributed to the long electron exposures of 960 s. These long electron exposures may be needed to reach saturation and desorb the CO and NO ligands over a significant fraction of the electron beam distribution on the surface.

The saturation behavior and corresponding high growth rates revealed from the results in Fig. 7 indicate that EE-ALD could be very useful. However, the long electron exposures of 960 s per reaction cycle required to obtain saturation behavior and high growth rates at incident electron currents of 21 μA from the electron flood gun do not facilitate rapid Co growth. Much higher incident electron currents are needed to produce Co film growth in more reasonable times. A higher current electron source, such as a hollow cathode plasma electron source, could be employed to address this issue.[25]

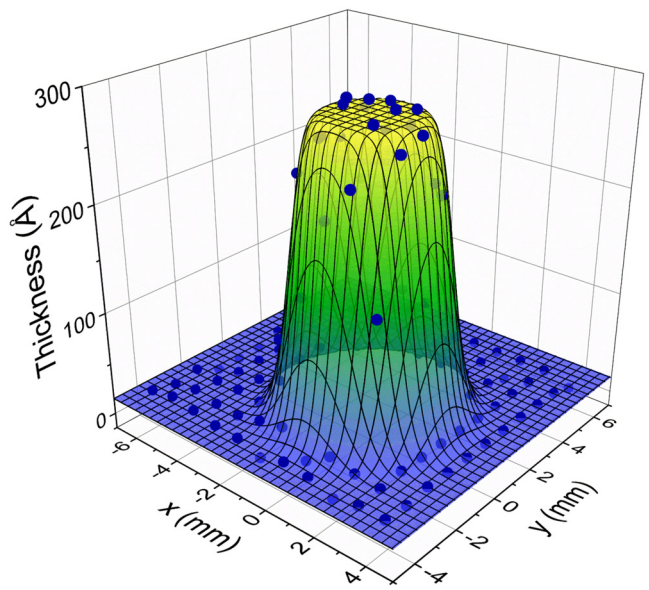

FIG. 7. Spatial map of the Co film on a silicon wafer as measured by *ex situ* spectroscopic ellipsometry. A distinctive flat top is observed on the Co film deposition. Co film thickness of ~289 Å is measured after 198 reaction cycles with an electron energy of 200 eV.

D. Film composition

The composition of the Co films was examined using *ex situ* XPS. These XPS measurements utilized the same Co film that was used for the spatial profile shown in Fig. 7. The *ex situ* XPS analysis was performed after the Co film had been exposed to atmosphere. The XPS depth profile analysis of the Co film is shown in Fig. 8. After a sputter time of 990 s, the XPS measurements revealed that the composition of the films was 51.6 at. % Co, 41.7 at. % O, and 6.7 at. % N. The samples contained a large amount of oxygen impurities because the Co films are easily oxidized in air.

The C XPS signal was below the XPS threshold intensity after sputtering into the Co film. The N/Co XPS signal ratio of 6.7 at. %/51.6 at. % = 0.13 indicates that approximately 13% of the nitrosyl ligands on the CTN precursors that lead to Co deposition are dissociated during the electron

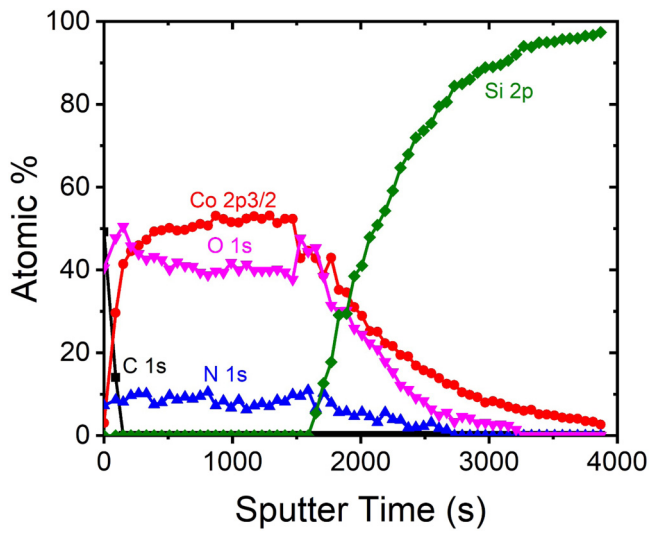

FIG. 8. Atomic percentage vs sputter time during XPS depth profile analysis of the Co film shown in Fig. 7.

exposures at 200 eV. In contrast, the lack of C XPS signals argues that the carbonyl ligands on CTN are desorbed cleanly during the electron exposures at 200 eV.

These XPS results for the Co film composition are fairly similar to earlier studies of Co FEBID using CTN and much higher electron energies of 5–20 keV. There was nitrogen in these Co depositions at 12–20 at. % and smaller levels of carbon at ≤10 at. %.[16,26] Additional studies have also explored electron beam induced reactions in CTN multilayers at −168 °C using lower electron energies of 500 eV.[17] These investigations are consistent with NO dissociation and CO desorption during electron irradiation.[17] After longer electron exposures at 500 eV, the partially decarbonylated Co species undergo electron stimulated CO decomposition.[17] The remaining CO species and most of the dissociated carbon atoms then leave the surface after annealing to room temperature.[17]

For the current studies, there is less NO dissociation and no observed CO decomposition after electron exposures at 200 eV for CTN adsorbed on the Co films at room temperature. These differences may result from the lower electron energy of 200 eV. The different behaviors may also be attributed to the lower coverages of the adsorbed CTN on the Co films at room temperature. Additional experiments at various temperatures, surface coverages, and electron energies are required to understand the film composition resulting from electron induced processes.

The high resolution Co 2p XPS signal obtained after 990 s of sputtering into the Co film is displayed in Fig. 9. This XPS spectrum is consistent with cobalt in the 2+ oxidation state.[27] The peaks were fit with features for Co $2p_{3/2}$, Co $2p_{1/2}$, shake-up satellites, and Co LMM Auger signals. Each of the Co 2p peaks was fit with two peaks to account for multiplet splitting.[27,28] The strong intensity of the Co shake-up satellites relative to their Co 2p transitions is indicative of Co(II) oxide.[27,28] The binding energies of the two Co $2p_{3/2}$ peaks are 782.6 and 779.8. These peak positions are in agreement with CoO.[27]

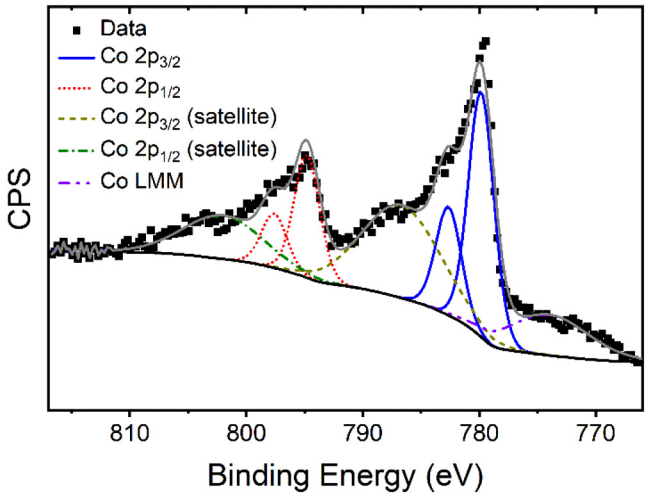

FIG. 9. Counts per second vs binding energy for the Co 2p XPS signal obtained after 990 s of sputtering into the Co film shown in Fig. 8. Peaks were fit using Co $2p_{3/2}$, Co $2p_{1/2}$, shake-up satellites and Co LMM Auger features.

There may also be a contribution shown in Fig. 9 from some Co(III) species. The possible presence of Co(III) oxides, such as Co_2O_3 and Co_3O_4, is complicated by the susceptibility of these oxides to ion induced reduction during sputtering.[29] More accurate compositional analysis of the Co films prior to atmospheric exposure must be performed using *in situ* techniques such as *in situ* Auger electron spectroscopy. The Auger spectrometer in the analysis chamber was not operational during the course of these experiments.

E. Electron induced desorption cross section from film spatial profile

The spatial profile shown in Fig. 7 was used to calculate the electron induced desorption cross section. The time-dependent surface coverage for a monolayer during electron induced desorption with a uniform electron flux can be modeled as[10,11,30]

$$\Theta(t) = \Theta_0 \exp[-(J\sigma/q\ A)t]. \quad (1)$$

In this expression, J is the electron current, A is the area of the irradiated surface, q is the charge of an electron, and σ is the total cross section for electron induced desorption. Θ_0 corresponds to the initial surface coverage of CO and NO species from the adsorbed CTN.

The Co atom coverage, X(t), deposited during one reaction cycle is proportional to the number of open sites on the surface resulting from the time-dependent electron induced desorption of CO and NO species. The Co atom coverage can be expressed as[10,11]

$$X(t) \sim (1\ -\Theta(t)). \quad (2)$$

The thickness of the Co film, T(t), can then be described as[10,11]

$$T(t) = \alpha(1 - \Theta(t)). \quad (3)$$

In this expression, α is a constant that includes the number of reaction cycles and the conversion between Co atom coverage deposited per reaction cycle and the Co film thickness deposited per reaction cycle. This conversion could also account for the expansion of the Co film upon atmospheric oxidation to form CoO.

The electron beam from the electron flood gun has a Gaussian profile. The electron flux from a normalized 2D-Gaussian is[11]

$$J[x, y] = J_0 \frac{1}{2\pi w_x w_y} \exp\left[-\frac{(x-x_c)^2}{2w_x^2} - \frac{(y-y_c)^2}{2w_y^2}\right]. \quad (4)$$

Inserting this expression for the electron flux in Eq. (1) yields an expression for the thickness of the oxidized Co film corresponding to different positions on the spatial profile of the electron beam. The resulting expression for the spatial distribution of the film thickness is[11]

$$T[x, y] = \alpha\left(1 - \exp\left[-t\frac{\sigma}{q}J_0\frac{1}{2\pi w_x w_y}\exp\left[-\frac{(x-x_c)^2}{2w_x^2} - \frac{(y-y_c)^2}{2w_y^2}\right]\right]\right) + T_0. \quad (5)$$

The offset, T_0, accounts for deposition outside of the primary electron beam.

Equation (5) can be fit to the spatial profile of the film shown in Fig. 7. The fitting parameters were α, σ, the center of the Gaussian profile at x_c and y_c, the width of the Gaussian profile determined by w_x and w_y, and T_0. This fit to the spatial profile yielded the electron induced desorption cross section. The best fit was consistent with a cross section of $\sigma = 2 \times 10^{-17} \pm 6 \times 10^{-18}$ cm^2. In addition, $\alpha = 269 \pm 12$ Å, $w_x = 0.70 \pm 0.05$ cm, $w_y = 0.70 \pm 0.05$ cm, and $T_0 = 15 \pm 4$ Å. The low background thickness of $T_0 = 15$ Å may be film growth resulting from secondary electron scattering.

F. Measured and predicted CO throughput during electron irradiation

The ESD cross section can be used to compare the measured and predicted CO throughput during electron irradiation. The mass spectrometer results shown in Fig. 3 can be employed to estimate the partial pressures of gaseous species by converting the ion currents to pressures. The mass spectrometer calibration yielded a conversion factor of 5×10^{-4} A/Torr for CO. The pressure increase produced by the electron current shown in Fig. 3 was then determined by dividing the increase in the ion current by the conversion factor. For the ion current increase of 0.17×10^{-12} A for the m/z = 28 signal (CO) in Fig. 3 during electron irradiation, the pressure increase is $\Delta P = 3.4 \times 10^{-10}$ Torr.

The CO pressure increase can then be employed to calculate the CO throughput, Q. This calculation uses the relationship $Q = S\Delta P$, where S is the pumping speed. Given S = 250 l/s for CO and $\Delta P = 3.4 \times 10^{-10}$ Torr, a CO throughput of $Q = 3.0 \times 10^{12}$ CO/s is obtained from the ~0.5 cm^2 electron irradiated area. The measured CO throughput can then be compared with the predicted CO throughput defined as the desorption of CO ligands per second from the ~0.5 cm^2 electron irradiated area.

The electron current on the sample in Fig. 3 is 45 μA over an area of ~0.5 cm^2. The electron flux can be obtained using the relationship $\Phi = I/Aq$, where Φ is the electron flux, I is the electron current, A is the irradiated area, and q is the electron charge. Based on this relationship, the electron flux is $\Phi = 5.6 \times 10^{14}$ electrons/(cm^2 s). The ESD cross section of 2.0×10^{-17} cm^2 can then be used to predict the CO throughput.

The normalized CO coverage, Θ/Θ_0, will be reduced by CO ESD according to $\Theta/\Theta_0 = \exp[-\sigma D]$.[10,11,30] In this expression similar to Eq. (1), D is the electron dose defined as the product of the electron flux, Φ, and time. For an exposure of 1 s, the electron dose is $D = 5.6 \times 10^{14}$ electrons/(cm^2 s) $\times 1$ s $= 5.6 \times 10^{14}$ electrons/cm^2. This electron dose for 1 s yields a normalized CO coverage of $\Theta/\Theta_0 = 0.989$. Likewise, 1.1% of the CO ligands are desorbed in 1 s.

The absolute CO coverage can then be estimated from the growth rate and the composition of the resulting cobalt film. A growth rate of 1.5 Å/cycle was obtained from the *ex situ* spectroscopic ellipsometry results in Fig. 7 assuming no nucleation period. The composition of these cobalt films was CoO after oxidation resulting from the atmospheric exposure. Using a CoO density of 6.44 g/cm^3, the growth rate of 1.5 Å/cycle is equivalent to 7.76×10^{14} CoO units/(cm^2 cycle).

Given three CO ligands per $Co(CO)_3NO$ precursor, there are 2.3×10^{15} CO ligands/cm^2 on the surface after $Co(CO)_3NO$ exposures, which yields a growth rate of 1.5 Å/cycle. This estimate assumes that the Co film deposited in vacuum was converted to a CoO film after oxidation by atmospheric exposure. If the electron exposures over 0.5 cm^2 for 1 s desorb 1.1% of this CO coverage, the CO throughput is 1.3×10^{13} CO/s. This predicted CO throughput of 1.3×10^{13} CO/s can be compared with the measured CO throughput of 3.0×10^{12} CO/s. The prediction of the CO throughput from the ESD cross section and the estimated CO absolute surface coverage is within a factor of 4 of the measured CO throughput. This agreement is good given all the assumptions and estimates used to obtain this comparison between the measured and predicted CO throughput during electron irradiation.

G. Comparison between spatial profiles for electron current and Co deposition

Figure 10 displays a cross section of the spatial profile of the film thickness from Eq. (5) that fits the individual film thicknesses displayed in Fig. 7. Figure 10 also shows the spatial profile of the Gaussian electron beam that fits the deposition results in Fig. 7. Individual film thicknesses measured

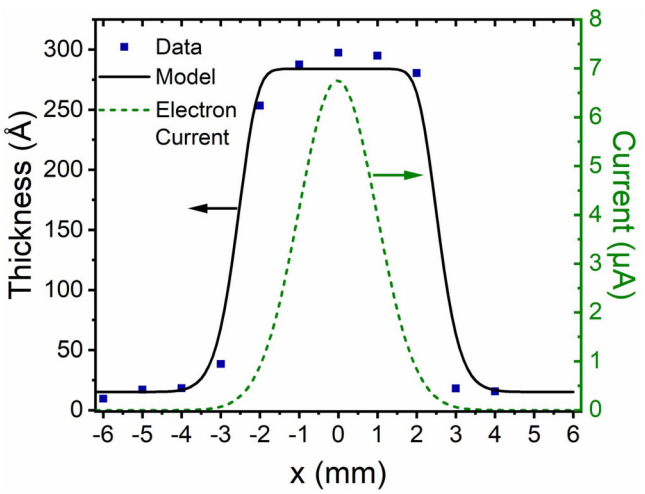

FIG. 10. Spatial profiles of the Gaussian electron beam and Co deposition for results in Fig. 7. Flat top on Co deposition extends over the central area of the electron beam.

through a cross section of the deposited film are also displayed in Fig. 10. The width of the Gaussian profile of the electron beam is smaller than the diameter of the film visible on the silicon wafer. A comparison between the spatial profiles of the electron beam and deposition reveals that the flat top of the film is obtained over a significant fraction of the electron beam.

The distinctive flat top on the Co deposition indicates that saturation was achieved over the central area of the electron beam for the long electron exposure times of 960 s used to obtain the spatial profiles shown in Figs. 7 and 10. Calculations can be performed to predict the spatial profile of the deposition for different electron exposure times assuming the reaction conditions in Fig. 7 with a cross section of $\sigma = 2 \times 10^{-17}\,\mathrm{cm}^2$. These predictions for electron exposure times from 15 to 3840 s are shown in Fig. 11. The thicknesses are normalized to the thickness obtained at saturation when electron induced desorption removes nearly all of the CO and NO surface species during the electron exposures.

Figure 11 shows that electron exposures <240 s do not display saturation behavior or obtain the maximum film thickness per reaction cycle. Longer electron exposures >240 s progressively reach larger amounts of saturation. These longer electron exposures produce the maximum film thickness per reaction cycle over a greater fraction of the spatial profile of the electron beam. Consequently, the size of the flat top area is larger with increasing electron exposure times.

H. Electron induced desorption cross section

The electron induced desorption cross section of $\sigma = 2 \times 10^{-17}\,\mathrm{cm}^2$ for Co growth is in good agreement with measured electron induced desorption cross sections derived from other recent film growth studies. An electron induced desorption cross section of $\sigma = 5.8 \times 10^{-17}\,\mathrm{cm}^2$ was measured for hydrogen desorption from Si during Si EE-ALD at 100 eV.[10] An electron induced desorption cross section of $\sigma = 4.2 \times 10^{-17}\,\mathrm{cm}^2$ was measured for hydrogen desorption from borazine during BN EE-ALD at 100 eV.[11] These cross sections are all higher than typical ESD cross sections of $\sigma = 10^{-23}$–$10^{-20}\,\mathrm{cm}^2$ that have been measured for the desorption of ionic species and $\sigma = 10^{-20}$–$10^{-18}\,\mathrm{cm}^2$ that have been reported for the desorption of neutral species.[1,31] These cross sections from recent film growth studies are also slightly smaller than typical cross sections of $\sim 10^{-16}\,\mathrm{cm}^2$ that have been reported for EID at 100 eV.[1]

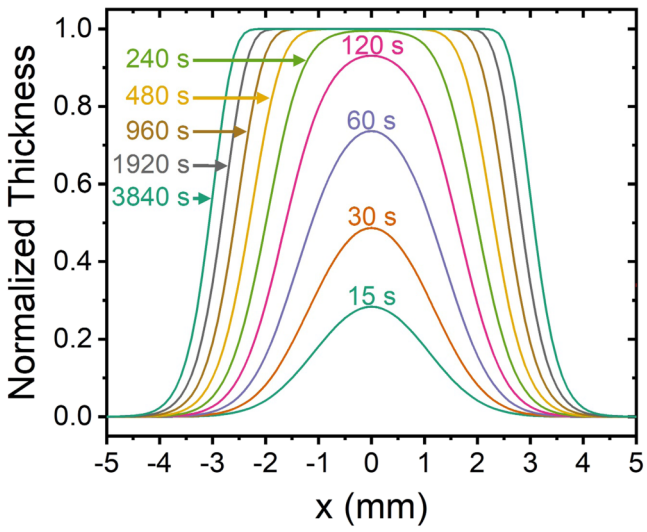

FIG. 11. Predicted spatial profile of Co deposition vs electron exposure time using an electron induced cross section obtained from results in Fig. 7. Saturation behavior is observed for electron exposure times ≥240 s.

This electron induced desorption cross section of $2 \times 10^{-17}\,\mathrm{cm}^2$ can also be compared with the cross sections for EID for the gas phase CTN that have been performed in the electron energy range from 0 to 140 eV.[22] These measurements observe the dissociation ionization of CTN with a threshold at an electron energy of ~20 eV. The highest cross section of $4.5 \times 10^{-16}\,\mathrm{cm}^2$ is observed for Co^+ production at electron energies from 50 to 100 eV.[22] The next highest cross section of $2.5 \times 10^{-16}\,\mathrm{cm}^2$ is measured for $[CoCO]^+$ production. A cross section of $1.0 \times 10^{-16}\,\mathrm{cm}^2$ is determined for $[Co(CO)_2NO]^+$ production.[22]

The fairly close agreement between the electron induced desorption cross section from this study and the absolute cross sections for the EID of the gas phase CTN suggests that CTN adsorbs as a physisorbed molecule on the Co surface. The adsorbed CTN precursor may not be significantly perturbed by the Co surface. The adsorbed CTN then undergoes ligand loss by mechanisms similar to the dissociative ionization of the gas phase CTN.

The dependence of the absolute cross sections on the electron energy for the dissociative ionization of the gas phase CTN is also fairly similar to the dependence of the electron induced desorption cross section on the electron energy that is shown in Fig. 5. The electron induced desorption cross section increases with the electron energy and peaks at 125 eV as displayed in Fig. 5. The cross section then decreases at higher electron energies. In comparison, the absolute cross sections for the dissociative ionization of the gas phase CTN have a threshold at ~20 eV, display their maximum values at electron energies of 50–100 eV, and then decrease for electron energies >100 eV.[22]

Although the Co growth rate versus electron energy shown in Fig. 5 is comparable to the dissociative ionization cross section for the gas phase CTN versus electron energy, there is still a possibility that the desorption of CO and NO ligands during Co growth could be dependent on low energy secondary electrons that are produced by the primary electrons. The electron beam induced deposition of Pt from methylcyclopentadienyl-platinum-trimethyl ($MeCpPtMe_3$) has been studied at electron energies from 40 to 1000 eV.[32] The results for Pt deposition yield versus electron energy displayed a maximum at 140 eV. The increasing Pt yield versus electron energies up to 140 eV and then decreasing yield at electron energies >140 eV are similar to the results observed for Co deposition in Fig. 5.[32]

The Pt deposition results from $MeCpPtMe_3$ have been explained in terms of the primary electrons inducing secondary electrons at <20 eV.[32,33] These secondary electrons

can then decompose the $MeCpPtMe_3$ via the DEA mechanism. However, there is ambiguity because the EID cross sections and the secondary electron emission yields both have their maximum values at electron energies of 80–150 eV.[2,34] Identifying whether the electron enhanced Pt deposition from $MeCpPtMe_3$ occurs through the EID or the DEA mechanism is not straightforward. Similar uncertainty exists for the electron enhanced growth of cobalt in this study.

IV. CONCLUSIONS

Cobalt thin films were deposited at room temperature using sequential cobalt tricarbonyl nitrosyl (CTN, $Co(CO)_3NO$) and low energy (75–175 eV) electron exposures from an electron flood gun. During this electron enhanced growth process, the CTN molecules were first adsorbed on the substrate. The carbonyl and nitrosyl ligands from the adsorbed CTN were then removed by electron induced desorption. New adsorption sites were produced by the removal of the CO and NO ligands. These new adsorption sites on the substrate allowed additional CTN to adsorb during subsequent CTN exposures.

The film thickness during the electron enhanced growth was monitored using *in situ* ellipsometry. Depending on the reaction conditions, the Co growth rates were as large as 1.3 Å/cycle. Using equivalent reaction conditions at lower incident electron currents, the maximum growth rate was measured at an electron energy of 125 eV. The CTN adsorption and the removal of the carbonyl and nitrosyl ligands could also be observed using *in situ* ellipsometry. The desorption of CO and NO during electron exposures was also confirmed using quadrupole mass spectrometer measurements.

XPS measurements revealed that the Co films were easily oxidized after atmospheric exposure. XPS analysis also detected some N in the Co film produced during electron exposures at 200 eV. The N/Co XPS signal ratio was consistent with the dissociation of 13% of the NO ligands on the CTN precursors that produce the Co film. The absence of C XPS signals from the Co films indicated that the CO ligands on CTN were completely desorbed by the electron exposures at 200 eV.

The Co films were deposited only on the surface area illuminated by the electron beam. The spatial profile of the Co film was mapped by *ex situ* spectroscopic ellipsometry. A distinctive flat top was observed for the spatial profile that was consistent with the electron induced desorption of nearly all the CO and NO surface coverage from the central area of the electron beam. Fitting the spatial profile of the Co film yielded an electron induced desorption cross section of $\sigma = 2 \times 10^{-17}$ cm^2 at 200 eV. This cross section is only slightly less than the cross sections for the EID of CTN in the gas phase. The dependence of the electron induced desorption cross section on electron energy was also similar to the electron energy dependence of the EID cross section for CTN in the gas phase. This agreement suggests that CTN is adsorbed on the Co surface as a nearly unperturbed, physisorbed molecule.

There is some ambiguity about the electron induced mechanism for Co growth. The electron energy dependence of the secondary electron yield is similar to the electron energy dependence of EID of CTN. The primary electrons could be directly causing EID or ESD via the Menzel–Gomer–Redhead or the Knotek–Feibelman mechanism. Alternatively, the primary electrons could be generating secondary electrons that then lead to dissociation of CTN via a DEA mechanism.

ACKNOWLEDGMENTS

This research was performed as part of the ASCENT (Applications and Systems Driven Center for Energy-Efficient Integrated Nanotechnologies) SRC JUMP Center. This work was supported in part by the Semiconductor Research Corporation (SRC) and Defense Advanced Research Projects Agency (DARPA).

[1]I. Utke, P. Hoffmann, and J. Melngailis, J. Vac. Sci. Technol. B **26**, 1197 (2008).
[2]W. F. van Dorp and C. W. Hagen, J. Appl. Phys. **104**, 081301 (2008).
[3]R. M. Thorman, T. P. R. Kumar, D. H. Fairbrother, and O. Ingolfsson, Beilstein J. Nanotechnol. **6**, 1904 (2015).
[4]W. F. van Dorp, A. Beyer, M. Mainka, A. Golzhauser, T. W. Hansen, J. B. Wagner, C. W. Hagen, and J. T. M. De Hosson, Nanotechnology **24**, 345301 (2013).
[5]D. Menzel and R. Gomer, J. Chem. Phys. **41**, 3311 (1964).
[6]M. L. Knotek and P. J. Feibelman, Phys. Rev. Lett. **40**, 964 (1978).
[7]S. Engmann, M. Stano, S. Matejcik, and O. Ingolfsson, Angew. Chem. Int. Ed. **50**, 9475 (2011).
[8]W. F. van Dorp, J. D. Wnuk, J. M. Gorham, D. H. Fairbrother, T. E. Madey, and C. W. Hagen, J. Appl. Phys. **106**, 074903 (2009).
[9]J. K. Sprenger, A. S. Cavanagh, H. Sun, K. J. Wahl, A. Roshko, and S. M. George, Chem. Mater. **28**, 5282 (2016).
[10]J. K. Sprenger, H. Sun, A. S. Cavanagh, and S. M. George, J. Vac. Sci. Technol. A **36**, 01A118 (2018).
[11]J. K. Sprenger, H. X. Sun, A. S. Cavanagh, A. Roshko, P. T. Blanchard, and S. M. George, J. Phys. Chem. C **122**, 9455 (2018).
[12]N. Bekiaris *et al.*, *Proceedings of 2017 IEEE International Interconnect Technology Conference (IITC)*, Hsinchu, Taiwan, 16–18 May 2017 (IEEE Publishing, New York, NY, 2017).
[13]J. Wu, W. F., S. Branagan, H. Suzuki, and J. van Eisden, J. Electrochem. Soc. **166**, D3136 (2019).
[14]A. R. Ivanova, G. Nuesca, X. M. Chen, C. Goldberg, A. E. Kaloyeros, B. Arkles, and J. J. Sullivan, J. Electrochem. Soc. **146**, 2139 (1999).
[15]P. A. Lane, P. E. Oliver, P. J. Wright, C. L. Reeves, A. D. Pitt, and B. Cockayne, Chem. Vap. Deposition **4**, 183 (1998).
[16]G. C. Gazzadi, H. Mulders, P. Trompenaars, A. Ghirri, M. Affronte, V. Grillo, and S. Frabboni, J. Phys. Chem. C **115**, 19606 (2011).
[17]S. G. Rosenberg, M. Barclay, and D. H. Fairbrother, J. Phys. Chem. C **117**, 16053 (2013).
[18]F. Vollnhals, M. Drost, F. Tu, E. Carrasco, A. Spath, R. H. Fink, H. P. Steinruck, and H. Marbach, Beilstein J. Nanotechnol. **5**, 1175 (2014).
[19]J. Postler, M. Renzler, A. Kaiser, S. E. Huber, M. Probst, P. Scheier, and A. M. Ellis, J. Phys. Chem. C **119**, 20917 (2015).
[20]J. Opitz, Int. J. Mass Spectrom. **225**, 115 (2003).
[21]P. Papp, S. Engmann, M. Kucera, M. Stano, S. Matejcik, and O. Ingolfsson, Int. J. Mass Spectrom. **356**, 24 (2013).
[22]S. Engmann, M. Stano, P. Papp, M. J. Brunger, S. Matejcik, and O. Ingolfsson, J. Chem. Phys. **138**, 044305 (2013).
[23]J. A. Venables, Surf. Sci. **299**, 798 (1994).
[24]L. Baker, A. S. Cavanagh, D. Seghete, S. M. George, A. J. M. Mackus, W. M. M. Kessels, Z. Y. Liu, and F. T. Wagner, J. Appl. Phys. **109** (2011).

[25]E. M. Oks and P. M. Schanin, Phys. Plasmas **6**, 1649 (1999).
[26]J. J. L. Mulders, L. M. Belova, and A. Riazanova, Nanotechnology **22**, 055302 (2011).
[27]M. C. Biesinger, B. P. Payne, A. P. Grosvenor, L. W. M. Lau, A. R. Gerson, and R. S. Smart, Appl. Surf. Sci. **257**, 2717 (2011).
[28]D. Briggs and V. A. Gibson, Chem. Phys. Lett. **25**, 493 (1974).
[29]V. S. Smentkowski, Prog. Surf. Sci. **64**, 1 (2000).
[30]T. E. Madey and J. T. Yates, J. Vac. Sci. Technol. **8**, 525 (1971).
[31]T. E. Madey, Science **234**, 316 (1986).
[32]A. Botman, D. A. M. de Winter, and J. J. L. Mulders, J. Vac. Sci. Technol. B **26**, 2460 (2008).
[33]T. E. Allen, R. R. Kunz, and T. M. Mayer, J. Vac. Sci. Technol. B **6**, 2057 (1988).
[34]W. F. van Dorp, Phys. Chem. Chem. Phys. **14**, 16753 (2012).